Analytica Chimica Acta 1235 (2022) 340536

Contents lists available at ScienceDirect

Analytica Chimica Acta

journal homepage: www.elsevier.com/locate/aca

# Sensitive detection of organophosphorus pesticides based on the localized surface plasmon resonance and fluorescence dual-signal readout

Kan Wang [a], Qian Li [b], Yan Wang [a], Yuanyuan Wu [a], Zewen Liu [a,*], Songqin Liu [c]

[a] Key Laboratory of Integrated Management of Crop Diseases and Pests (Ministry of Education), College of Plant Protection, Nanjing Agricultural University, Nanjing, 210095, People's Republic of China
[b] School of Food Science and Engineering, Yangzhou University, Huayang Xilu 196, Yangzhou, Jiangsu, 225127, People's Republic of China
[c] State Key Laboratory of Bioelectronics, Jiangsu Engineering Laboratory of Smart Carbon-Rich Materials and Device, School of Chemistry and Chemical Engineering, Southeast University, Nanjing, 211189, People's Republic of China

## HIGHLIGHTS

- A novel LSPR/FL dual-signal visual biosensor is firstly reported for OPs detection.
- Ag/Au NPs-based multifunctional nanoprobe is designed with dual-readout performance.
- $H_2O_2$ act as a bifunctional moderator to change the LSPR/FL signal of nanoprobe.
- Two distinct LSPR/FL spectra and color changes increased the OPs detection accuracy.
- This work hold great potential for OPs detection in real sample.

## GRAPHICAL ABSTRACT

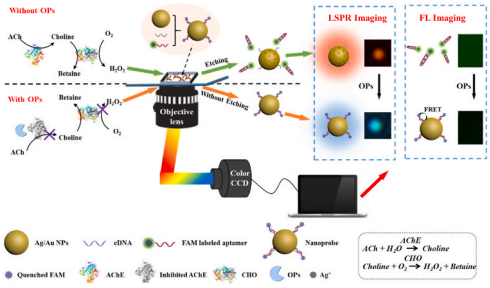


## ARTICLE INFO

*Keywords:*
Dual-signal visual detection
Ag/Au nanoparticle
Organophosphorus pesticide
Localized surface plasmon resonance
Fluorescence

## ABSTRACT

In this work, a dual-signal visual biosensor was designed for organophosphorus pesticides (OPs) detection using DNA functionalized Ag/Au bimetallic nanoparticles (Ag/Au NPs) as multifunctional nanoprobe. The dual-signal detection strategy was based on the inhibition of enzyme-induced $H_2O_2$ generation by OPs in the detection solution containing acetylcholinesterase (AChE), choline oxidase (CHO), acetylcholine (ACh) and nanoprobe. $H_2O_2$ produced by enzyme-catalyzed reaction could trigger the etching of Ag and dissociation of carboxy-fluorescein (FAM)-labeled aptamer from the nanoprobe, resulting in significant localized surface plasmon resonance (LPRR) and fluorescence (FL) signal responses. In the presence of OPs, AChE activity was inhibited to disrupt the enzymatic generation of $H_2O_2$, which allowed to simultaneous quantitative measure OPs through the LSPR peak shifts and FL intensity variations of the nanoprobe. The LSPR/FL dual-signal biosensor showed great selectivity and sensitivity for OPs detection. In addition, two distinct colour changes were visually observed to match the LSPR/FL spectra signal responses, which was a feasible means for visual analysis of OPs. Consequently, the work provided a dual-signal visual biosensor via the combination of multifunctional nanoprobe, and had significant potential to monitor pesticide residue with high anti-interference capability and detection accuracy.

* Corresponding author.
*E-mail address:* liuzewen@njau.edu.cn (Z. Liu).

https://doi.org/10.1016/j.aca.2022.340536
Received 13 August 2022; Received in revised form 12 October 2022; Accepted 16 October 2022
Available online 21 October 2022

## 1. Introduction

Organophosphorus pesticides (OPs) have been used extensively to increase the quality of agriculture produce and minimize the loss of crops [1,2]. In spite of significant economic benefits in food production, the inevitable OPs residues result in various unavoidable adverse effects and persistent damage on environment, ecosystem, and human health [3,4]. For instance, OPs could accumulate in the human body, resulting in irreversible harm to multiple organs even at trace levels [5,6]. Consequently, establishment of a rapid and ultrasensitive assay for OPs is an urgent demand for human safety. A variety of detection methods have been developed to identify OPs such as capillary electrophoresis, chromatography, mass spectrometry, fluorescence (FL), colorimetric, and chemiluminescence techniques with excellent performance [7–11]. However, most methods are single-signal sensors which can be influenced by many factors like instrument conditions, environmental fluctuations and interference, giving rise to false-positive or false-negative problems in practical applications.

In recent years, the construction of dual-signal sensor through the combination of two different signal readout for a single target determination has attracted considerable attention, which greatly improve the anti-interference capability and detection accuracy for practical application [12–17]. Currently, several dual-signal biosensors to pesticides have been proposed based on the integration of surface-enhanced Raman scattering (SERS), electrochemiluminescence (ECL), FL and colorimetric techniques [18–20]. For example, Zhao et al. designed a colorimetric/SERS dual-signal sensor using gold nanoparticles coupled with polymers for atrazine sensitive detection in apple juice [21]. He et al. designed a dual-signal ECL nanoprobe using L-CdS QDs as cathodic and c-PFBT NPs as anodic probe for OPs analysis [22]. These dual-signal biosensors have enabled good selectivity, high sensitivity, multi-response, and accurate detection for pesticides, owing to the self-calibration and mutual verification by two different signals. In addition, Zha et al. proposed a FL/colorimetric dual-modal immunosensor with o-phenylenediamine and gold nanostars as reaction substrates for detecting chloroacetamide [23]. Liang et al. established a FL/colorimetric dual-signal visual sensor for malathion detection using gold nanoparticles and carbon quantum dots as nanoprobes [24]. The FL/colorimetric sensor is a pioneering way for pesticides detection based on two kind of color changes, which possess advantages like dual-signal visualization, prompt response, small sample dose demand, and easy operation. However, these reported dual-signal sensor commonly utilizes two individual readout probes, which might complicate the manipulation procedure and led to unpredictable interference. Besides that, the relatively low sensitivity and weak signal readout of colorimetric technique still restrict the trace detection of pesticides residues. Therefore, the combination of novel optical technologies and design of a multimodality nanoprobe with dual-readout performance for OPs visualization detection are particularly promising.

As a novel visual detection technique, the localized surface plasmon resonance technique (LSPR) has garnered considerable attention in biochemical detection and cell imaging with high signal-to-noise ratio and remarkable optical performance [25–27]. The LSPR signal is closely related to the nanoparticle size, morphology, composition, and surrounding dielectric environment [28,29]. Additionally, the LSPR technique can recognize scattering light of nanoparticle at single particle level, which provide higher spatiotemporal resolution and sensitivity than those of traditional average measuring technique [30,31]. Noble metal nanoparticles are ideal LSPR nanoprobes owing to their good biocompatibility, low toxicity, strong scattering signal and photostability [32,33]. Moreover, due to the feasible functionalization and strong capability of signal transduction, numerous noble metal nanoparticles-based FL nanoprobes have been developed for visualization biosensor [34,35]. These unique characteristics of noble metal nanoparticles enable the possibility of building a multimodality nanoprobe with LSPR and FL dual-signal readout for visualization detection.

Based on the above, we have developed a LSPR and FL dual-signal biosensor for rapid detection and imaging of OPs using DNA-functionalized Ag/Au bimetallic nanoparticles (Ag/Au NPs) as multifunctional nanoprobe. Bimetallic nanoparticles exhibit superior chemical and physical properties to monocomponent nanoparticles, which can greatly improve the detection selectivity and sensitivity. The established LSPR/FL biosensor was firstly reported for visual detection of OPs based on a multifunctional nanoprobe integrating two kinds of signal changes, which could obtain multiscale information for accurate quantify of OPs.

## 2. Experimental

### 2.1. Reagents

Acetylcholine chloride (ACh), acetylcholinesterase (AChE), choline oxidase (CHO), bis(*p*-sulfonatophenyl)phenylphosphine (BSPP), chlorpyrifos (a model for OPs detection), ascorbic acid (AA) were obtained from Sigma-aldrich (China). 10 mM of PBS phosphate buffer buffer solution (pH 7.4), $Ag^+$ aptamer: 5′-FAM- CCT CCC TCC TTT TCC ACC CAC C -3′ and complementary DNA (cDNA): 5′–SH–GGT GGG TG-3′ were obtained from Sangon Biotech (China). Hydroxylamine hydrochloride ($NH_2OH{\bullet}HCl$), trisodium citrate, chloroauric acid tetrahydrate ($HAuCl_4{\bullet}4H_2O$), hydrogen peroxide ($H_2O_2$), silver nitrate ($AgNO_3$) and other reagents were purchased from Sinopharm Chemical Reagent (China).

### 2.2. Apparatus

UV–vis spectra were performed with a Shimadzu UV-2450 spectrophotometer (Japan). Transmission microscope (TEM) images were recorded on a JEOL JEM-2100 (Japan). An Olympus microscope IX73 equipped with a 60X objective lens (NA = 0.7), a dark-field condenser (0.8 < NA<0.92) and a colour charge coupled Olympus DP80 CCD (Japan) were acquired for Dark field measurements (DFM) images and fluorescence (FL) images. LSPR scattering spectra were operated with a FERGIE spectrometer and IX73 using a Princeton 400BR EMCCD as detector (USA). FL spectra were acquired on a Horiba FluoroMax-4 spectrophotometer (USA).

### 2.3. Preparation of Ag/Au bimetallic nanoparticles and nanoprobe

The template silver nanoparticles (Ag NPs) was according to previous method: briefly, $AgNO_3$ (0.125 mL, 0.2 M) solution was added to 50 mL of water with vigorous stirring. After boiling, sodium citrate (3 mL, 1%) solution was added, followed by addition of AA (2 mL, 0.1 M) solution. After heating for 8 min, centrifugation and washing, the resultant Ag nanoparticles was re-dispersed in water.

The preparation of Ag/Au NPs was according to previous method [36] : the above prepared Ag NPs solution ($1.5 \times 10^{11}$ particles $mL^{-1}$, 5 mL) was diluted with water (5 mL), after boiling, $HAuCl_4$ (0.1 wt%, 100 μL) and $NH_2OH{\cdot}HCl$ (20 mM, 100 μL) was added and stirred for 8 min. The Ag/Au NPs was thus obtained and stored (4 °C) for the follow experiment.

For cDNA and aptamer coupling, BSPP was added to Ag/Au NPs (1 mL) solution, and incubation at room temperature overnight. Then, BSPP modified Ag/Au NPs was mixed with cDNA (5 μL, 100 μM) and rocked 48 h. After washing, aptamer (5 μL, 100 μM) was added and incubated for 5 h. The cDNA and aptamer co-functionalized Ag/Au NPs nanoprobe was re-dispersed in PBS buffer (1 mL, pH 7.4) and stored (4 °C) for further uses.

### 2.4. Determination OPs by LSPR and FL

Different concentrations of pesticides (20 μL) were mixed with AChE (20 μL, 0.8 mU $mL^{-1}$) and incubated for 30 min at 37 °C. After that, CHO

(20 μL, 10 mU $mL^{-1}$) and ACh (40 μL, 0.2 mM) were added for 30 min. Later, as-synthesized nanoprobe (100 μL, 0.1 nM) was added and reacted at room temperature for 30 min. The LSPR spectra of the resulting mixtures were obtained with our previous method [37,38]. The FL spectra of the resulting mixtures were obtained with excitation at 495 nm. Meanwhile, an inverted microscope was used for the DFM and FL imaging.

## 3. Results and discussion

### 3.1. Characterizations of the nanoprobe

Ag/Au NPs was prepared with Ag NPs as template, and using colloid seed-mediated replacement and deposition reactions. The template Ag NPs with 50 nm of average diameter had an extinction peak of 430 nm (Fig. S1 and S2). TEM image displayed that Ag/Au NPs had a uniform size, good monodispersity, hollow and intact with mostly round shape (Fig. 1A). UV–*vis* spectra showed that the obtained Ag/Au NPs possessed a maximum absorption peak of 465 nm. After cDNA and aptamer coupling on the Ag/Au NPs via Au–S bond and DNA hybridization, the as-prepared DNA functionalized nanoprobe had two characteristic absorption peaks: 260 nm corresponding to the absorbance of DNA, and 465 nm attributing to the absorbance of Ag/Au NPs (Fig. 1B). The successful DNA surface modification of nanoprobe was also confirmed by a more negative charge than the Ag/Au NPs (Fig. 1C) using Zeta potential measurements. The LSPR signal of nanoprobe was corroborated by Dark-field imaging and LSPR scattering spectra. An apparent cyan scattering light was observed in the Dark-field image due to the LSPR performance of Ag/Au NPs (Fig. 1D). The LSPR scattering spectra of the both nanoprobe and Ag/Au NPs exhibited an evident LSPR peak at 500 nm, indicated that the DNA assembly had negligible LSPR changes (Fig. 2A). A strong fluorescence at 518 nm of FAM-labeled aptamer could be observed, but the fluorescence at 518 nm of nanoprobe was decreased dramatically (Fig. 2B). The quenched FL of nanoprobe was due to the fluorescence resonance energy transfer (FRET) process between Ag/Au NPs (acceptor) and FAM (donor). All these observations demonstrated the successful formation of the nanoprobe.

### 3.2. Feasibility of OPs detection using the nanoprobe

The principle for OPs detection was produced in Scheme 1. The thiolated cDNA and FAM-labeled aptamer were modified on Ag/Au NPs to obtain nanoprobe, which emitted cyan scattering light and quenched FL. When ACh was added to AChE + nanoprobe, or CHO + nanoprobe solution, no LSPR shift and FL changes were observed, indicating that $H_2O_2$ could not be created by single enzyme catalytic reaction (Figs. S3 and S4). Upon addition of ACh to AChE + CHO + nanoprobe, AChE hydrolyze ACh to form choline that was subsequently oxidized by CHO to generate $H_2O_2$. $H_2O_2$ etched Ag in nanoprobe, which caused the change of the local dielectric environment, making a tremendous LSPR peak shift from 500 to 635 nm along with scattering color change from cyan to red (Fig. 2A and C). Meanwhile, the generated $Ag^+$ would react with its aptamer to form $Ag^+$-Apt complex [39], which led to the discharge of aptamer on the nanoprobe and the recovering of FL at 518 nm (Fig. 2B). When OPs were mixed with AChE, and then added CHO, ACh and nanoprobe, AChE activity was irreversibly inhibited by OPs and decreased the generation of choline [5,9], thus preventing the production of $H_2O_2$ to etch Ag. As a result, the scattering color and the LSPR peak remained unchange or change slightly (Fig. 2A and C). At the same time, the existence of OPs led to almost no fluorescence (Fig. 2B). Control experiment was evaluated using cDNA and aptamer co-functionalized Ag NPs and Au NPs with diameter of 50 nm instead of Ag/Au NPs. Notably, DNA functionalized bimetallic Ag/Au NPs as nanoprobe exhibited improved optical performance for LSPR sensing, because of the more distinct color difference (Fig. 2C).

The etching Ag by the enzymatic cascade reaction was demonstrated by TEM analysis and energy-dispersive X-ray spectroscopy (EDX) measurement. As expected, the as-prepared nanoprobe was a complete shell with the elements coexisting Au/Ag bimetallic nature (89 atom% Ag and 11 atom% Au) before enzymatic reaction occurred (Fig. 3A). After

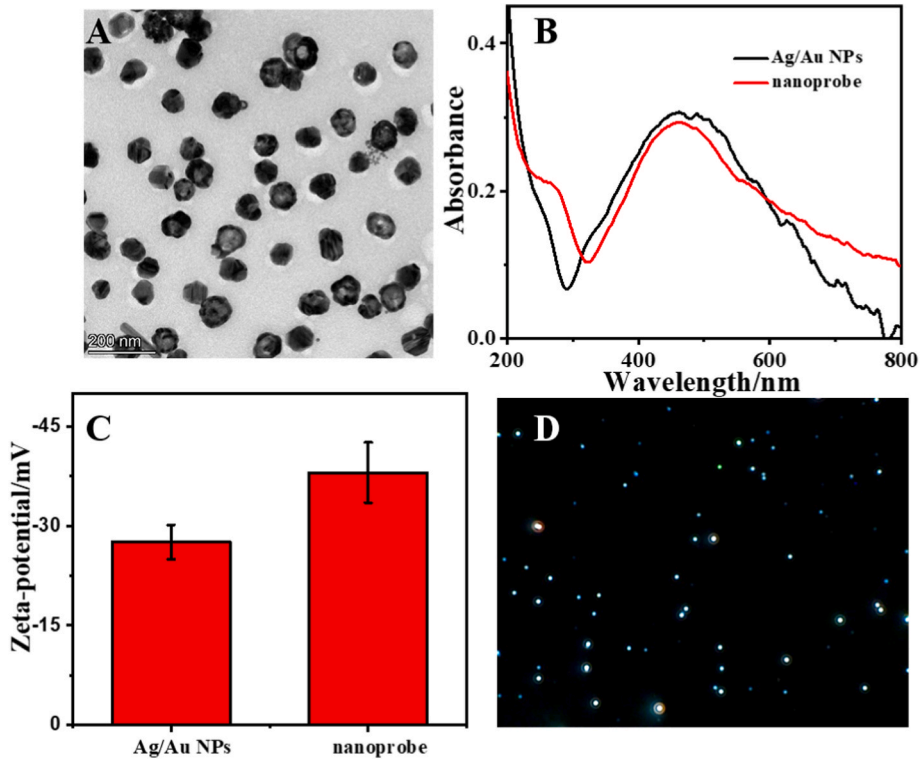


**Fig. 1.** (A) TEM images of Ag/Au NPs. (B) UV–vis spectra of Ag/Au NPs and nanoprobe. (C) Zeta potentials of Ag/Au NPs and nanoprobe. (D) Dark-field images of nanoprobe.

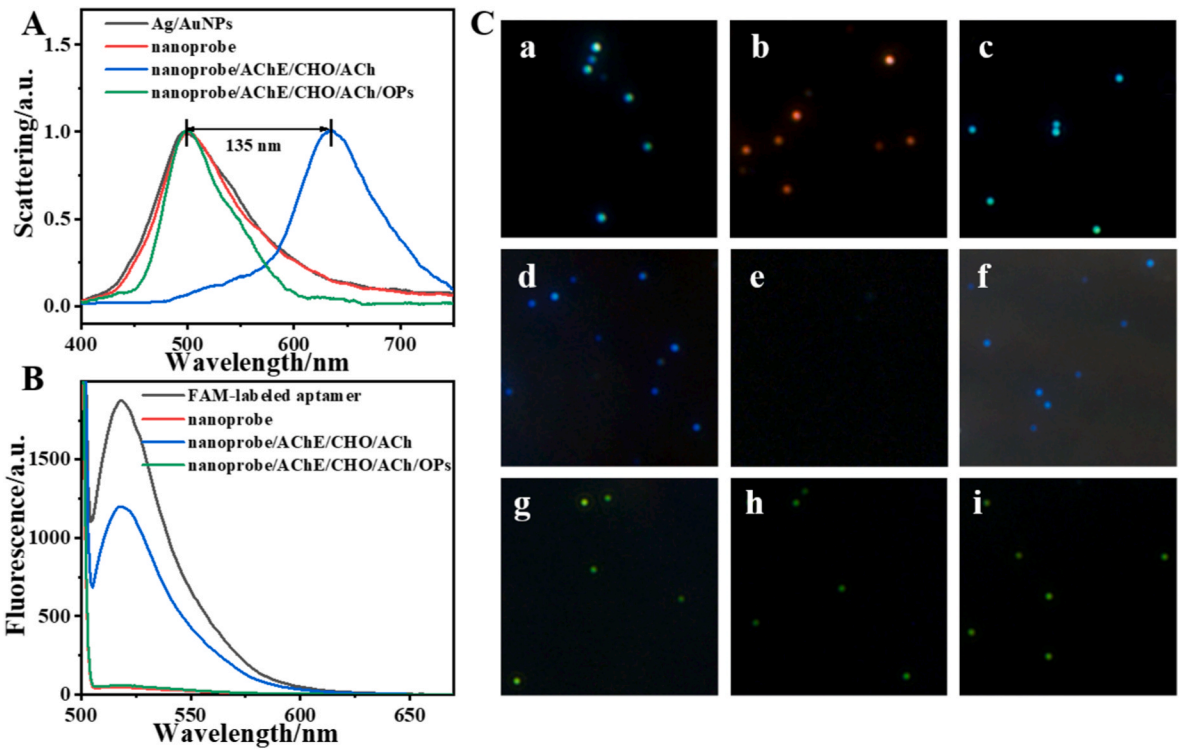


**Fig. 2.** (A) LSPR scattering spectra (B) Fluorescence spectra of Ag/Au NPs, aptamer, nanoprobe, nanoprobe + AChE + CHO + ACh and nanoprobe + AChE + CHO + ACh + OPs. (C) Dark-field images of (a) nanoprobe, (b) nanoprobe + AChE + CHO + ACh, (c) nanoprobe + AChE + CHO + ACh + OPs, (d) DNA functionalized Ag NPs, (e) DNA functionalized Ag NPs + AChE + CHO + ACh, (f) DNA functionalized Ag NPs + AChE + CHO + ACh + OPs, (g) DNA functionalized Au NPs, (h) DNA functionalized Au NPs + AChE + CHO + ACh, (i) DNA functionalized Au NPs + AChE + CHO + ACh + OPs. $C_{AChE} = 0.8$ mU mL$^{-1}$, $C_{CHO} = 10$ mU mL$^{-1}$, $C_{ACh} = 0.2$ mM, $C_{OPs} = 500$ ng mL$^{-1}$.

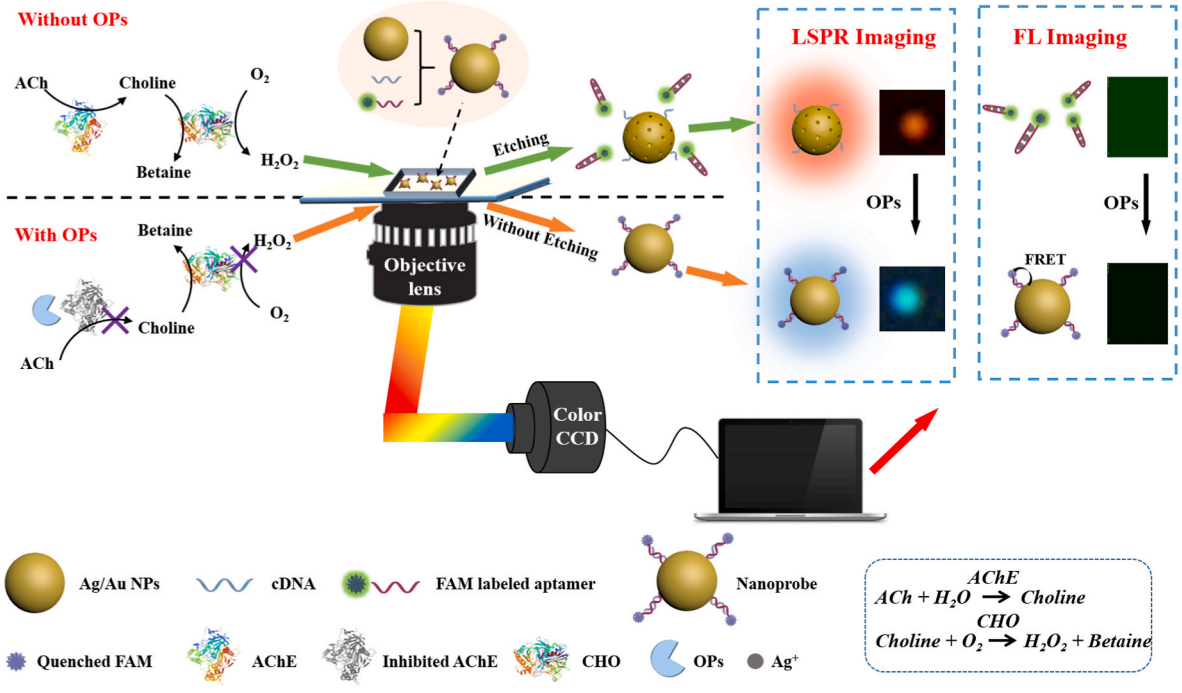


**Scheme. 1.** Schematic illustration of the OPs dual-signal sensor.

incubating with AChE and adding CHO and ACh, EDX analysis of the nanoprobes also showed that the Ag percentage (77 atom % Ag and 23 atom % Au) was lower than that of the nanoprobes, indicating that the enzyme induced $H_2O_2$ etching process (Fig. 3B). In the presence of OPs, the corresponding TEM displayed similar morphology as nanoprobe itself, but the Ag percentage (88 atom% Ag and 12 atom% Au) was slightly lower than that of the nanoprobes (Fig. 3C), indicating the successful inhibition of the activity of AChE by OPs. Furthermore, the

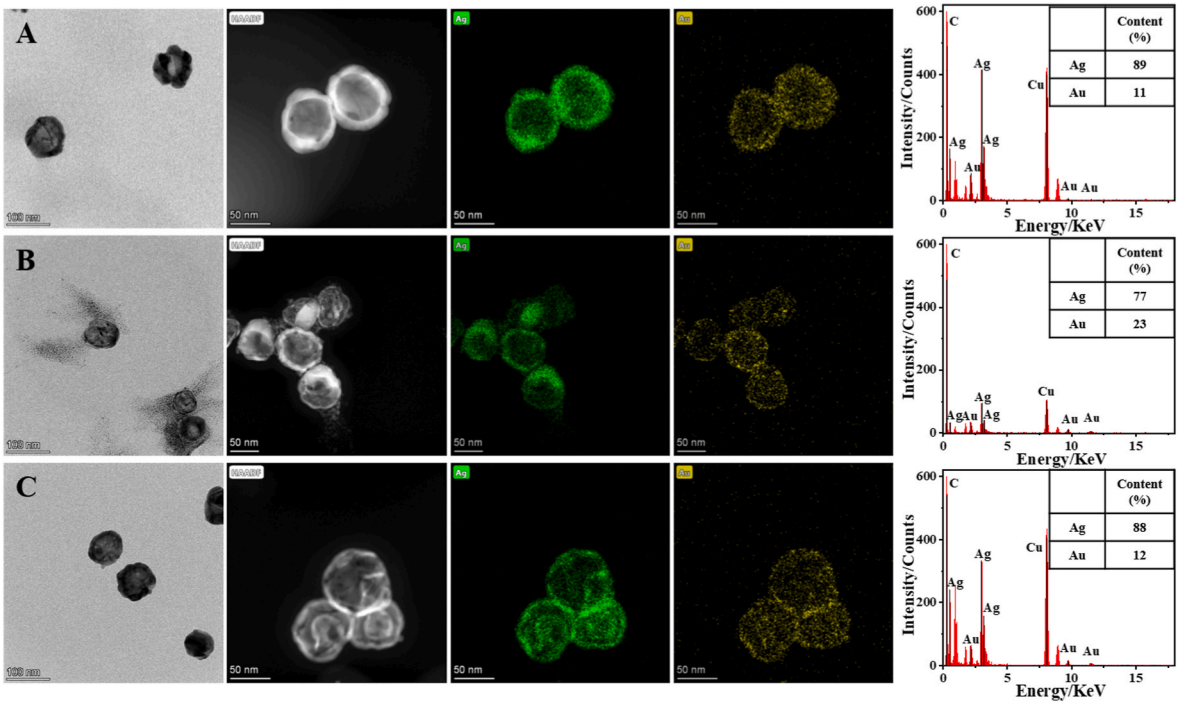


**Fig. 3.** TEM images, medium angle annular dark field images, TEM elemental mappings of Ag and Au, and corresponding EDX spectra of (A) nanoprobe, (B) nanoprobe + AChE (0.8 mU $mL^{-1}$) + CHO (10 mU $mL^{-1}$) + ACh (0.2 mM), (C) nanoprobe + AChE (0.8 mU $mL^{-1}$) + CHO (10 mU $mL^{-1}$) + ACh (0.2 mM) + OPs (500 ng $mL^{-1}$).

inhibition efficiency of AChE activity depended on the concentration of OPs and the reaction time. This allowed us to develop a sensing strategy to detect and image of OPs based on nanoprobe and LSPR/FL dual-signal monitoring.

### 3.3. The optimization of important parameters

Several important experimental parameters were evaluated to obtain the best performance for OPs analysis, including AChE concentrations, incubation time, and pH of detection solution were evaluated. Various concentrations of AChE were added into nanoprobe + CHO + ACh solution to evaluate the effects of AChE concentrations. As shown from the LSPR and FL spectra, the peak shift and FL intensity was increased in the presence of 0–0.8 mU $mL^{-1}$ of AChE, and more AChE would resulted in the peak shift and FL intensity leveled off (Figs. S5 and S6). Therefore, 0.8 mU $mL^{-1}$ of AChE was adopted for OPs assay. In addition, after incubation of OPs with AChE and then added into nanoprobe + CHO + ACh, both the LSPR peak shift and quenched FL intensity remarkably increased and achieve the maximum at pH 7.4 (Figs. S7 and S8). Therefore, pH 7.4 was an optimal buffer solution condition. On other hand, the LSPR peak shift increased with reaction time, and peak shift leveled off after 20 min (Fig. S9). And the quenched fluorescence intensity in sensing system at 518 nm reached maximum and leveled off after 30 min (Fig. S10). Thus, 30 min was chosen as optimal reaction time for OPs determination.

### 3.4. Detection of OPs using LSPR and FL spectra

The OPs dose-dependent response was investigated by scattering spectra and DFM images. With the increase of OPs concentration (0–500 pg $mL^{-1}$), the LSPR peak of an individual nanoprobe in the detection solution blue-shifted from 635 nm to 500 nm (Fig. 4A). The peak shifts of nanoprobe were linearly with OPs concentration range from 1 to 500 pg $mL^{-1}$ with a detection limit of 0.33 pg $mL^{-1}$ (S/N = 3). The linear equation could be expressed by Y = 19.80 + 41.45 log(X) with $R^2$ = 0.969, Y and X represented the peak shift of nanoprobe in detection solution and OPs concentration, respectively (Fig. 4B). Simultaneously, the scattering color of the nanoprobe in the detection solution changed from red to green and to cyan finally (Fig. 4C). The remarkable scattering color changes initiated by OPs proposed a prominent capacity and novel LSPR visualization detection method for OPs. To explore the selectivity of the proposed method toward OPs detection, other pesticides including imidacloprid, clothianidin, deltamethrin, thiamethoxam, pymetrozine and acetamiprid should be tested, respectively. No obvious color changes and only small peak shifts were noticed upon introduction of the above control pesticides, which confirmed the good selectivity of the proposed LSPR sensing strategy for OPs detection (Fig. 4D).

Meanwhile, the FL spectra and corresponding FL images was also used to explore the OPs concentration response to aptamer discharge on nanoprobe. Upon the OPs concentration increase, the fluorescence intensity gradually decreased, which was a result of the highly specific aptamer-$Ag^+$ binding to dissociate FAM-labeled aptamer from the nanoprobe (Fig. 5A). The calibration curve in Fig. 5B had a linear relationship between the detection solution FL intensity ($F$) and the concentrations of OPs ($c$) over a range of 5–500 ng $mL^{-1}$. The linear equation could be represented as $F$ = 1289.63–467.43 log($c$). The detection limit for OPs was 1.67 ng $mL^{-1}$ with $R^2$ = 0.988. Moreover, the green fluorescence of the detection solution faded away with the increase of OPs (Fig. 5C). The noticeable fluorescence color changes of the FRET-based FL sensing method showed a rapid and simple strategy for OPs visual detection. Receiver operating characteristic (ROC) curves were performed by using "non-OPs" as negative and "OPs" as positive. As shown in Fig. 5D, the area under the ROC curve (AUC) value was 0.979, representing the excellent OPs discrimination ability of the detection technique. The detection selectivity was studied further by the comparison of the fluorescence quenching value ($\Delta F = F - F_0$) with the addition of OPs and other pesticides. $F$ and $F_0$ was the fluorescence intensity of the detection solution before and after the addition of OPs or other pesticides. As shown in Fig. S11, the FL signal changes of other pesticides were negligible, indicating the high specificity of the proposed FL sensing strategy for OPs detection. To demonstrate the

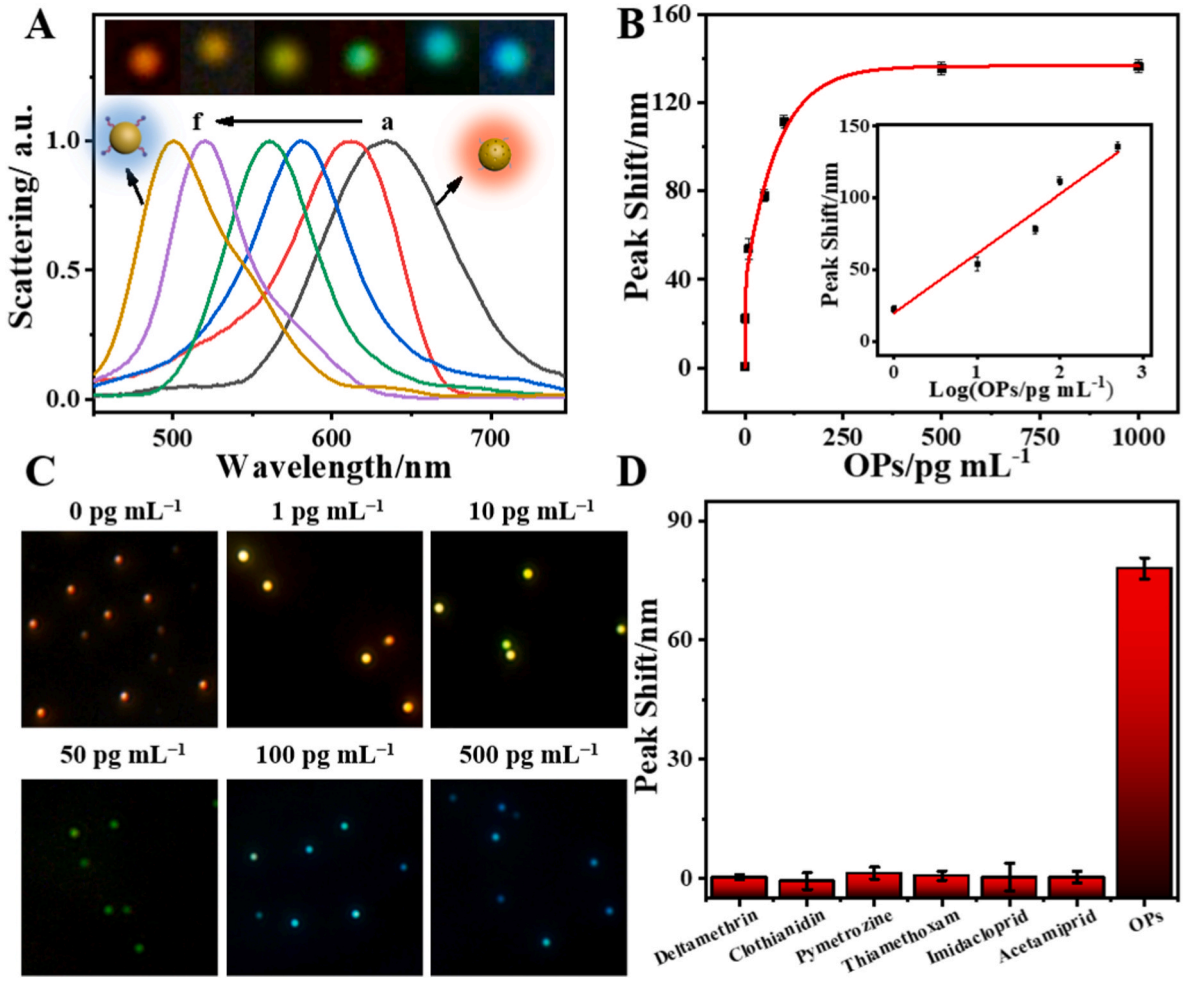


**Fig. 4.** (A) LSPR scattering spectra and Dark-field images of an individual nanoprobe + AChE (0.8 mU $mL^{-1}$) + CHO (10 mU $mL^{-1}$) + ACh (0.2 mM) upon exposure to OPs (a to f: 0, 1, 10, 50, 100, and 500 pg $mL^{-1}$). (B) Linear relationship at OPs concentration range from 1 to 500 pg $mL^{-1}$. (C) Corresponding Dark-field images of nanoprobe + AChE (0.8 mU $mL^{-1}$) + CHO (10 mU $mL^{-1}$) + ACh (0.2 mM) + OPs (OPs concentrations: 0, 1, 10, 50, 100, and 500 pg $mL^{-1}$). (D) Selective experiment of nanoprobe + AChE (0.8 mU $mL^{-1}$) + CHO (10 mU $mL^{-1}$) + ACh (0.2 mM) with OPs (50 pg $mL^{-1}$) and interferents (5 μg $mL^{-1}$).

universality, other common OPs including demeton, malathion, dichlorvos, parathion and dimethoate were also selected for detection. From the corresponding LSPR peak shifts and fluorescence quenching value of nanoprobe in Figs. S12 and S13, these OPs possess different inhibition ability toward AChE for the disparities of molecular characteristics. Therefore, the established dual-signal sensor could be applied for most of OPs detection. Moreover, the analytical performance of the developed dual-signal method was compared with other reported methods (Table S1). Both the sensing modes exhibited higher or comparable sensitivities relative to most other existed sensors. The dual-signal sensor provided more options for OPs detection, and double checked the results to reduce the background interference and improve the accuracy than single-signal sensor. Furthermore, the dual-signal sensor combined LSPR and FL signal could be used for simultaneous visualization assay, and was beneficial to the sensitive and rapid OPs detection.

### 3.5. Accuracy assay of OPs using real samples

To evaluate the practical application of the developed sensor, a standard addition means of OPs was used for water samples from Nanjing City. The collected tap water and lake water were centrifuged for 20 min and filtered with a 0.22 μm membrane filter before spiked with different concentrations of OPs. Results were shown in Table 1, the recoveries for OPs using the LSPR technique varied from 91% to 96% with the relative standard deviation (RSD) less than 5.8%. Meanwhile, the FL technique also showed good precision for spiked OPs with the recoveries ranging from 92% to 98% and the RSD lower than 3.2%. The high recovery and accuracy of the proposed LSPR/FL dual-signal OPs sensor indicated a good feasibility and great potential for real samples detection.

## 4. Conclusions

In conclusion, the work produced a novel LSPR/FL dual-signal strategy for the detection of OPs. Based on the inhibition activity of AChE by OPs to prevent the enzymatic $H_2O_2$ generation, the interruption of Ag etching and FAM-labeled aptamer releasing processes from nanoprobe were applied for OPs detection with LSPR and FL method. The nanoprobe LSPR shift and FL intensity variation before and after AChE inhibition by OPs was achieved for OPs quantitatively measuring. Meanwhile, OPs visualization imaging was remarkably improved for two distinguishable scattering and fluorescence color changes in detection solution. The established LSPR/FL biosensor for OPs detection was successfully applied in real water sample with high sensitivity and selectivity. Therefore, the dual-signal visual detection strategy clearly demonstrated great potential for pesticides residues quantitative and visual screening.

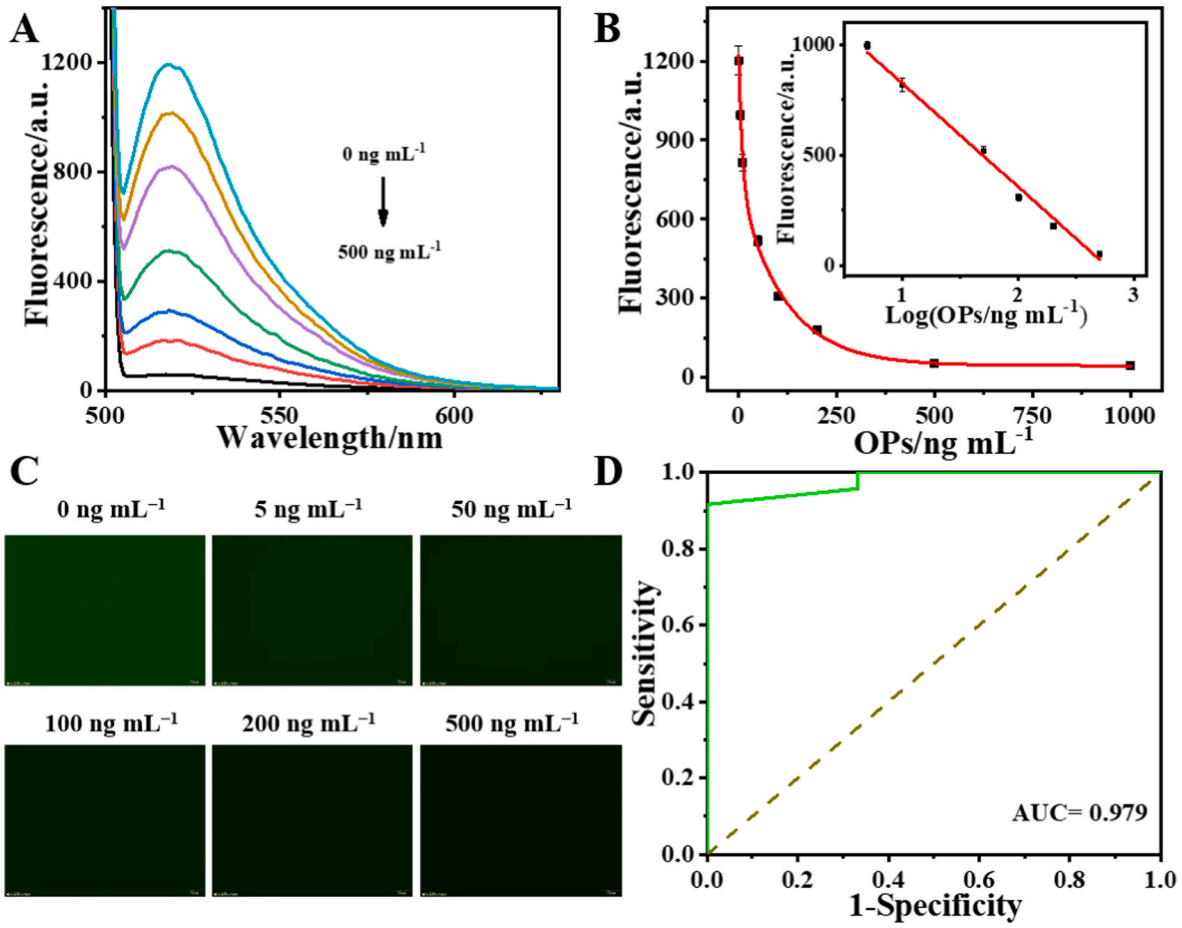


**Fig. 5.** (A) Fluorescence spectra of nanoprobe + AChE (0.8 mU $mL^{-1}$) + CHO (10 mU $mL^{-1}$) + ACh (0.2 mM) upon exposure to OPs (0, 5, 10, 50, 100, 200, and 500 ng $mL^{-1}$). (B) Linear relationship at OPs concentration from 5 to 500 ng $mL^{-1}$ (C) Corresponding fluorescence images of nanoprobe + AChE (0.8 mU $mL^{-1}$) + CHO (10 mU $mL^{-1}$) + ACh (0.2 mM) + OPs (OPs concentrations: 0, 5, 50, 100, 200, and 500 ng $mL^{-1}$). (D) The corresponding ROC analysis for the discrimination of OPs.

**Table 1**
Assay results for OPs detection in real water samples (n = 3).

| Samples | LSPR | | | | FL | | | |
|---|---|---|---|---|---|---|---|---|
| | Added (pg $mL^{-1}$) | Found (pg $mL^{-1}$) | Recovery (%) | RSD (%) | Added (ng $mL^{-1}$) | Found (ng $mL^{-1}$) | Recovery (%) | RSD (%) |
| Lake water | 10 | 9.3 | 93 | 3.3 | 10 | 9.4 | 94 | 2.5 |
| | 100 | 96 | 96 | 5.8 | 100 | 97 | 97 | 3.2 |
| | 500 | 480 | 96 | 3.5 | 500 | 490 | 98 | 2.0 |
| Tap water | 10 | 9.1 | 91 | 4.0 | 10 | 9.2 | 92 | 3.2 |
| | 100 | 92 | 92 | 2.7 | 100 | 94 | 94 | 2.7 |
| | 500 | 476 | 95 | 1.3 | 500 | 482 | 96 | 2.0 |

## CRediT authorship contribution statement

**Kan Wang:** Writing – original draft, Data curation, Visualization. **Qian Li:** Conceptualization, Investigation. **Yan Wang:** Formal analysis, Validation. **Yuanyuan Wu:** Investigation. **Zewen Liu:** Supervision, Resources. **Songqin Liu:** Writing – review & editing.

## Declaration of competing interest

The authors declare that they have no known competing financial interests or personal relationships that could have appeared to influence the work reported in this paper.

## Data availability

Data will be made available on request.

## Acknowledgements

This work was supported by Jiangsu Planned Projects for Postdoctoral Research Funds (2020Z302) and China Postdoctoral Science Foundation (2021T140333 and 2020M681647).

## Appendix A. Supplementary data

Supplementary data to this article can be found online at https://doi.org/10.1016/j.aca.2022.340536.

## References

[1] M. Liu, A. Khan, Z. Wang, Y. Liu, G. Yang, Y. Deng, N. He, Aptasensors for pesticide detection, Biosens. Bioelectron. 130 (2019) 174–184.

[2] L. Yang, Y.L. Liu, C.G. Liu, F. Ye, Y. Fu, Two luminescent dye@MOFs systems as dual-emitting platforms for efficient pesticides detection, J. Hazard Mater. 381 (2020), 120966.
[3] C. Li, H. Zhu, C. Li, H. Qian, W. Yao, Y. Guo, The present situation of pesticide residues in China and their removal and transformation during food processing, Food Chem. 354 (2021), 129552.
[4] V. Kumar, K. Vaid, S.A. Bansal, K.H. Kim, Nanomaterial-based immunosensors for ultrasensitive detection of pesticides/herbicides: current status and perspectives, Biosens. Bioelectron. 165 (2020), 112382.
[5] T. Yao, A. Liu, Y. Liu, M. Wei, W. Wei, S. Liu, Ratiometric fluorescence sensor for organophosphorus pesticide detection based on opposite responses of two fluorescence reagents to $MnO_2$ nanosheets, Biosens. Bioelectron. 145 (2019), 111705.
[6] J. Chen, X. Chen, Q. Huang, W. Li, Q. Yu, L. Zhu, S. Liu, Z. Chi, Amphiphilic polymer-mediated aggregation-induced emission nanoparticles for highly sensitive organophosphorus pesticide biosensing, ACS Appl. Mater. Interfaces 11 (2019) 32689–32696.
[7] X. Yan, H. Li, X. Su, Review of optical sensors for pesticides, Trac. Trends Anal. Chem. 103 (2018) 1–20.
[8] A. Samsidar, S. Siddiquee, S.M. Shaarani, A review of extraction, analytical and advanced methods for determination of pesticides in environment and foodstuffs, Trends Food Sci. Technol. 71 (2018) 188–201.
[9] R. Jin, D. Kong, X. Zhao, H. Li, X. Yan, F. Liu, P. Sun, D. Du, Y. Lin, G. Lu, Tandem catalysis driven by enzymes directed hybrid nanoflowers for on-site ultrasensitive detection of organophosphorus pesticide, Biosens. Bioelectron. 141 (2019), 111473.
[10] H. Li, D. Su, H. Gao, X. Yan, D. Kong, R. Jin, X. Liu, C. Wang, G. Lu, Design of red emissive carbon dots: robust performance for analytical applications in pesticide monitoring, Anal. Chem. 92 (2020) 3198–3205.
[11] H. Wu, J. Wu, H. Wang, Y. Liu, G. Han, P. Zou, Sensitive and label-free chemiluminescence detection of malathion using exonuclease-assisted dual signal amplification and G-quadruplex/hemin DNAzyme, J. Hazard Mater. 411 (2021), 124784.
[12] Z. Hao, X. Lin, J. Li, Y. Yin, X. Gao, S. Wang, Y. Liu, Multifunctional nanoplatform for dual-mode sensitive detection of pathogenic bacteria and the real-time bacteria inactivation, Biosens. Bioelectron. 173 (2021), 112789.
[13] S. Han, L. Yang, Z. Wen, S. Chu, M. Wang, Z. Wang, C. Jiang, A dual-response ratiometric fluorescent sensor by europium-doped CdTe quantum dots for visual and colorimetric detection of tetracycline, J. Hazard Mater. 398 (2020), 122894.
[14] J. Qian, C. Ren, C. Wang, K. An, H. Cui, N. Hao, K. Wang, Gold nanoparticles mediated designing of versatile aptasensor for colorimetric/electrochemical dual-channel detection of aflatoxin B1, Biosens. Bioelectron. 166 (2020), 112443.
[15] J. Zhang, H. Zhang, S. Ye, X. Wang, L. Ma, Fluorescent-Raman binary star ratio probe for microRNA detection and imaging in living Cells, Anal. Chem. 93 (2020) 1466–1471.
[16] J. Tang, L. Liu, J. Qin, X. Lv, J. Li, D. Tang, J. Zhuang, Biocatalysis-mediated MOF-to-prussian blue transformation enabling sensitive detection of NSCLC-associated miRNAs with dual-readout signals, Biosens. Bioelectron. 206 (2022), 114139.
[17] Z. Yu, G. Cai, X. Liu, D. Tang, Pressure-based biosensor integrated with a flexible pressure sensor and an electrochromic device for visual detection, Anal. Chem. 93 (2021) 2916–2925.
[18] Y. Chen, Y. Zhu, Y. Zhao, J. Wang, Fluorescent and colorimetric dual-response sensor based on copper (II)-decorated graphitic carbon nitride nanosheets for detection of toxic organophosphorus, Food Chem. 345 (2021), 128560.
[19] F.S. Belaïdi, L. Farouil, L. Salvagnac, P. Temple-Boyer, I. Séguy, J.L. Heully, F. Alary, E. Bedel-Pereira, J. Launay, Towards integrated multi-sensor platform using dual electrochemical and optical detection for on-site pollutant detection in water, Biosens. Bioelectron. 132 (2019) 90–96.
[20] H. Ouyang, X. Tu, Z. Fu, W. Wang, S. Fu, C. Zhu, D. Du, Y. Lin, Colorimetric and chemiluminescent dual-readout immunochromatographic assay for detection of pesticide residues utilizing g-$C_3N_4$/$BiFeO_3$ nanocomposites, Biosens. Bioelectron. 106 (2018) 43–49.
[21] B. Zhao, S. Feng, Y. Hu, S. Wang, X. Lu, Rapid determination of atrazine in apple juice using molecularly imprinted polymers coupled with gold nanoparticles-colorimetric/SERS dual chemosensor, Food Chem. 276 (2019) 366–375.
[22] Y. He, F. Hu, J. Zhao, G. Yang, Y. Zhang, S. Chen, R. Yuan, Bifunctional moderator-powered ratiometric electrochemiluminescence enzymatic biosensors for detecting organophosphorus pesticides based on dual-signal combined nanoprobes, Anal. Chem. 93 (2021) 8783–8790.
[23] Y. Zha, S. Lu, P. Hu, H. Ren, Z. Liu, W. Gao, C. Zhao, Y. Li, Y. Zhou, Dual-modal immunosensor with functionalized gold nanoparticles for ultrasensitive detection of chloroacetamide herbicides, ACS Appl. Mater. Interfaces 13 (2021) 6091–6098.
[24] N. Liang, X. Hu, W. Li, A.W. Mwakosya, Z. Guo, Y. Xu, X. Huang, Z. Li, X. Zhang, X. Zou, J. Shi, Fluorescence and colorimetric dual-mode sensor for visual detection of malathion in cabbage based on carbon quantum dots and gold nanoparticles, Food Chem. 343 (2021), 128494.
[25] X. Chen, Q. Xia, Y. Cao, Q. Min, J. Zhang, Z. Chen, H.Y. Chen, J.J. Zhu, Imaging the transient heat generation of individual nanostructures with a mechanoresponsive polymer, Nat. Commun. 8 (2017) 1–10.
[26] T. Xie, M. Li, Y.T. Long, Dual-channel signals for intracellular mRNA detection via a PRET nanosensor, Chem. Commun. 53 (2017) 7768–7771.
[27] J. Wang, Q. Yu, X.L. Li, X.L. Zhao, H.Y. Chen, J.J. Xu, A reversible plasmonic nanoprobe for dynamic imaging of intracellular pH during endocytosis, Chem. Sci. 13 (2022) 4893–4901.
[28] T.T. Zhai, D. Ye, Y. Shi, Q.W. Zhang, X. Qin, C. Wang, X.H. Xia, Plasmon coupling effect-enhanced imaging of metal ions in living cells using DNAzyme assembled core-satellite structures, ACS Appl. Mater. Interfaces 10 (2018) 33966–33975.
[29] Y. Ling, D. Zhan, X. Cui, M. We, T. Zhang, J. Wang, L. Xiao, Y. Xia, Direct monitoring of cell membrane vesiculation with 2D AuNP@$MnO_2$ nanosheet supraparticles at the single-particle level, Angew. Chem. Int. Ed. 58 (2019) 10542–10546.
[30] R. Niu, C. Song, F. Gao, W. Fang, X. Jiang, S. Ren, D. Zhu, S. Su, J. Chao, S. Chen, C. Fan, L. Wang, DNA origami-based nanoprinting for the assembly of plasmonic nanostructures with single-molecule surface-enhanced Raman scattering, Angew. Chem. Int. Ed. 60 (2021) 11695–11701.
[31] M.K. Song, Y.P. Ma, H. Liu, P.P. Hu, C.Z. Huang, J. Zhou, High resolution of plasmonic resonance scattering imaging with deep learning, Anal. Chem. 94 (2022) 4610–4616.
[32] Q. Zhang, H.H. Yan, C. Ru, F. Zhu, H.Y. Zou, P.F. Gao, C.Z. Huang, J. Wang, Plasmonic biosensor for the highly sensitive detection of microRNA-21 via the chemical etching of gold nanorods under a dark-field microscope, Biosens. Bioelectron. 201 (2022), 113942.
[33] C. Song, J. Zhang, X. Jiang, H. Gan, Y. Zhu, Q. Peng, X. Fang, Y. Guo, L. Wang, SPR/SERS dual-mode plasmonic biosensor via catalytic hairpin assembly-induced AuNP network, Biosens. Bioelectron. 190 (2021), 113376.
[34] Y. Wu, M.R. Ali, K. Chen, N. Fang, M.A. El-Sayed, Gold nanoparticles in biological optical imaging, Nano Today 24 (2019) 120–140.
[35] J. Tao, X. Yu, Y. Guo, G. Wang, H. Ju, L. Ding, Proximity enzymatic glyco-remodeling enables direct and highly efficient lipid raft imaging on live cells, Anal. Chem. 92 (2020) 7232–7239.
[36] G. Qi, Y. Zhang, J. Wang, D. Wang, B. Wang, H. Li, Y. Jin, Smart plasmonic nanozyme enhances combined chemo-photothermal cancer therapy and reveals tryptophan metabolic apoptotic pathway, Anal. Chem. 91 (2019) 12203–12211.
[37] K. Wang, L. Jiang, F. Zhang, Y. Wei, K. Wang, H. Wang, Z. Qi, S. Liu, Strategy for in situ imaging of cellular alkaline phosphatase activity using gold nanoflower probe and localized surface plasmon resonance technique, Anal. Chem. 90 (2018) 14056–14062.
[38] K. Wang, F. Zhang, Y. Wei, W. Wei, L. Jiang, Z. Liu, S. Liu, In situ imaging of cellular reactive oxygen species and caspase-3 activity using a multifunctional theranostic probe for cancer diagnosis and therapy, Anal. Chem. 93 (2021) 7870–7878.
[39] Y. Wei, B. Li, X. Wang, Y. Duan, Magnified fluorescence detection of silver (I) ion in aqueous solutions by using nano-graphite-DNA hybrid and DNase I, Biosens, Bioelectron 58 (2014) 276–281.